Engineering Analysis with Boundary Elements 84 (2017) 117–128

Contents lists available at ScienceDirect

Engineering Analysis with Boundary Elements

journal homepage: www.elsevier.com/locate/enganabound

Improved numerical manifold method (iNMM)—An extra-DOF free and interpolating NMM with continuous nodal stress

Guohua Zhang, Yongtao Yang*, Hao Wang

State Key Laboratory of Geomechanics and Geotechnical Engineering, Institute of Rock and Soil Mechanics, Chinese Academy of Sciences, Wuhan 430071, China

ARTICLE INFO

Keywords:
Numerical manifold method
Partition of unity
Linear dependence
Extra DOFs
Continuous nodal stress
FE-Meshfree element

ABSTRACT

As a partition of unity method (PUM), the numerical manifold method (NMM) is capable of constructing global approximation by simply multiplying PU function with local approximation. In order to enhance accuracy, high order polynomials can be specified as local approximation. This, however, will hinder the engineering application of NMM by its ill conditioning of the global stiffness matrix. In this study, an improved NMM (iNMM) without extra degree of freedoms (DOFs) is developed. Without the extra DOFs, the resulting global stiffness becomes linear independent. In addition, the stresses are continuous at all nodes. Numerical studies show the iNMM's excellent accuracy.

1. Introduction

Over the past three decades, the concept of partition of unity (PU) approximations has been established and a number of PU-based methods [1] were developed for solid mechanics, such as the partition of unity method [2–5], the generalized finite element method [6], the extended finite element method (XFEM) [7,8], the numerical manifold method (NMM) [9,10], the phantom-node method [11,12] and many others [13–16].

Since the advent, the NMM has attracted much interest from researchers in computational solid mechanics as it possesses several advantages over the FEM. For example, the local approximation function in NMM can be freely chosen so as to obtain higher resolution of the boundary value problem. In addition, the mathematical mesh in NMM does not have to match the material interface or the fracture face, indicating that NMM can always employ regular mesh to discretize the problem domain. This, however, is nearly impossible for FEM, when dealing with problems with complicated geometric boundaries. According to our experience from isoparametric elements, such as four-node isoparametric quadrilateral element (Quad4) and eight-node isoparametric quadrilateral element (Quad8) [17], regular mesh can generally achieve much better accuracy than distorted mesh. Moreover, NMM is very suitable for simulating problems with moving boundaries, such as crack propagation problems, while in FEM, the mesh has to be ceaselessly regenerated so as to match the evolving fracture face. Due to the attractive advantages, NMM has been successfully used to model static crack propagation problems [18–23], dynamic crack propagation problems [24], contact problems [25] seepage problems [26,27] and wave propagation problems [28].

Within the framework of PU-based method, high-order global approximations can be directly constructed in the NMM by simply adopting high-order polynomial local approximations. Use of smooth polynomial local approximations can achieve the following purposes [29,30]: (1) perform *p*-adaptive analysis without the addition of extra nodes; (2) avoid mesh grading yet obtain a same quality of approximation on a uniform mesh; (3) remove global refinement constraints. However, when both the PU function and the local approximations are simultaneously taken as high-order polynomials, the resulting global stiffness matrix will be "linear dependence" (LD) and special equation solver is needed, because traditional equation solver generally designed for positive definite equations cannot solve singular equations. Here, the LD problem means the global stiffness matrix is still singular even after the basic boundary condition to eliminate the rigid body displacement has been imposed.

The LD problem was first observed by Babuška and Melenk [2,3] when they designed a one-dimensional PUM approximation for the one-dimensional Helmholtz equation. To address LD problem, great efforts have been made in the past years by various means. An et al. [31] proposed an algorithm for predicting the rank deficiency of the stiffness matrix by using the topological information inheriting in the finite element mesh. Griebel and Schweitzer [32] proposed flat-top PU functions to avoid the linear dependence problems. The only problem is the complexity involved in the construction of the flat-top PU functions [29]. Tian et al. [33] carried out numerical experiments among

* Corresponding author.
E-mail address: scuhhc@126.com (Y. Yang).

http://dx.doi.org/10.1016/j.enganabound.2017.08.011
Received 19 March 2017; Received in revised form 4 July 2017; Accepted 16 August 2017
Available online 31 August 2017
0955-7997/

several GFEMs to investigate the LD problem. Based on the numerical experiments, they proposed several approaches to eliminate the linear dependence problem, such as suppressing the higher-order degrees of freedom (DOF) and adjustment of the element geometry. However, as discussed in [34], these approaches [33] cannot ensure the removal of the LD problem and are also difficult to be implemented robustly in practice. In [34], Cai et al. developed a PU-based triangular element using a dual local approximation scheme by treating boundary and interior nodes separately. According to their report, the use of dual local approximation scheme can effectively remove the LD problem. Based on overlapping polyhedral covers generated from Voronoi cells, Riker and Holzer [35] proposed a mixed-cell-complex partition of unity method (MCCPUM) to eliminate the LD problem. However, the generation of mixed-cell-complex is very rather complicated and computationally expensive.

In other front, a family of PU-based "FE-Meshfree" elements was proposed in [36–39] which successfully eliminates the LD problem and the shape function possesses the desirable delta property. Although a least square version of point interpolation method (LSPIM) [36,37] or radial point interpolation method (RPIM) [40], which is time-consuming, is used to construct the local approximations of the "FE-Meshfree" elements, extra nodes or DOFs are not needed, because they just use the same mesh as in the FEM, and the total DOFs is the same as FEM. Numerical tests carried out in [36–38] have shown that the "FE-Meshfree" elements are computationally more efficient than FEM. If regular mesh is adopted, accuracy obtained through "FE-Meshfree" elements is much better than that obtained through FEM. If distorted mesh is adopted, FE-Meshfree elements have much better mesh-distortion tolerance than FEM.

Although high-order global approximations can be constructed easily in "FE-Meshfree" elements, the nodal stress is not continuous at nodes, and stress smoothing operation is needed in the post processing stage. To further improve the property of "FE-Meshfree" elements, Yang Zheng et al. [41–48] developed a series of "FE-Meshfree" elements with continuous nodal stress, such as the 'FE-Meshfree' three-node triangular element with continuous nodal stress using radial-polynomial basis functions (Trig3-RPIMcns) [48]. According to their report, Trig3-RPIMcns can obtain better accuracy, higher convergence rate and higher tolerance to mesh distortion than the three-node triangular elements (Trig3) and the four-node quadrilateral element (Quad4) for linear elastic, free vibration and forced vibration problems by simply using the same mesh as in Trig3. Since Trig3-RPIMcns has to deploy conforming mesh to discretize the problem domain, the time spent in mesh generation for problems with complex boundaries is not negligible. If crack propagation is involved, the burden of mesh generation is further amplified. This demerit hinders the applications of Trig3-RPIMcns for practical problems. Since there is no need for NMM to deploy conforming mesh, the mesh generation should be very convenient. Besides, NMM can always adopt regular mesh to discretize the problem domain, and mesh distortion, which results in poor accuracy for FEM, does not exist in NMM. Therefore, developing a method which combines the advantages of both the Trig3-RPIMcns and the NMM is essential.

In this study, an improved version of NMM (iNMM), which synergizes the advantages of both the Trig3-RPIMcns and the numerical manifold method (NMM), is developed for linear elastic problems. The property and performance of the iNMM will be studied in great detail in the rest of this paper. The outline of this paper is as follows: Section 2 briefly introduces the numerical manifold method (NMM); Section 3 presents the formulation of iNMM and the properties of the iNMM shape functions are discussed. Section 4 presents the discrete equations for linear elastic problems in the context of iNMM; Numerical examples and discussions are subsequently presented in Section 5. Some conclusions are drawn in the last section.

2. Basic concepts of NMM

The background of NMM has been described in great detail in [49]. Therefore, only the basic concepts are introduced in this section. To illustrate these concepts, an example shown in Fig. 1 is employed.

The core and most innovative feature of the NMM is the adoption of two cover systems, namely the mathematical cover (MC) and the physical cover (PC), from which the nodes and elements are generated.

The MC is the union of a series of user-defined overlapping small domains. Each small domain is called mathematical patch (MP). In Fig. 1, the MC is constructed by regular triangular mesh, and hence each MP is the union of several triangles sharing the same node such as MP_1. It is noticed that the MC does not have to match the material boundaries, holes or fracture faces of the problem domain, but have to cover the problem domain completely.

The PC is the union of all the physical patches (PPs). The PPs are generated by intersecting all the MPs with the physical mesh. Here, the physical mesh is the union of all the material interfaces, joints, fractures and domain boundaries, which are used to define the unique problem domain. From a MP, at least one PP can be generated, such as PP_2, PP_3, PP_4, and PP_5 (Fig. 1). It is noticed that each PP corresponds to a "NMM node" (also named as "generalized node"), on which the degree of freedoms (DOFs) are defined, such as GN_2^p in Fig. 1. In the rest of this paper, the "NMM node" will be simply called "node" for the purpose of description.

In NMM, the basic units to integrate the weak form of the problem are manifold elements. Each manifold element is the common domains of neighboring PPs, such as E_1, which is the common domains of PP_3, PP_4 and PP_5 (Fig. 1).

3. Formulation for the iNMM

In order to synergize the advantages of both the Trig3-RPIMcns and the numerical manifold method (NMM), an improved version of NMM (iNMM) is developed. Formulation of the iNMM will be described in great detail in this section.

As a PU-based method, the global approximation of NMM in a manifold element is obtained by multiplying the PU function with the local approximation, and expressed as

$$u^h(\boldsymbol{x}) = w_1(\boldsymbol{x})u_1(\boldsymbol{x}) + w_2(\boldsymbol{x})u_2(\boldsymbol{x}) + w_3(\boldsymbol{x})u_3(\boldsymbol{x}) \tag{1}$$

where $w_i(\boldsymbol{x})$ and $u_i(\boldsymbol{x})$ are the PU function and the local approximation function associated with physical patch i (PP_i), respectively.

3.1. PU function of the iNMM

The area coordinates are used to construct the PU functions of iNMM. The transformation of the area coordinates is defined as [50]:

$$\begin{bmatrix}1\\x\\y\end{bmatrix}=\begin{bmatrix}1 & 1 & 1\\x_1 & x_2 & x_3\\y_1 & y_2 & y_3\end{bmatrix}\begin{bmatrix}L_1\\L_2\\L_3\end{bmatrix},\quad \begin{bmatrix}L_1\\L_2\\L_3\end{bmatrix}=\frac{1}{2A}\begin{bmatrix}x_2y_3-x_3y_2 & y_2-y_3 & x_3-x_2\\x_3y_1-x_1y_3 & y_3-y_1 & x_1-x_3\\x_1y_2-x_2y_1 & y_1-y_2 & x_2-x_1\end{bmatrix}$$
$$\overset{\text{def}}{=\!=}\frac{1}{2A}\begin{bmatrix}a_1 & b_1 & c_1\\a_2 & b_2 & c_2\\a_3 & b_3 & c_3\end{bmatrix}\begin{bmatrix}1\\x\\y\end{bmatrix}, \tag{2}$$

in which

$$2A=\det\begin{bmatrix}1 & 1 & 1\\x_1 & x_2 & x_3\\y_1 & y_2 & y_3\end{bmatrix},\quad L_1+L_2+L_3=1. \tag{3}$$

Unlike traditional NMM, which uses the FEM shape functions to construct the PU functions, the PU functions of the iNMM are expressed as [48]

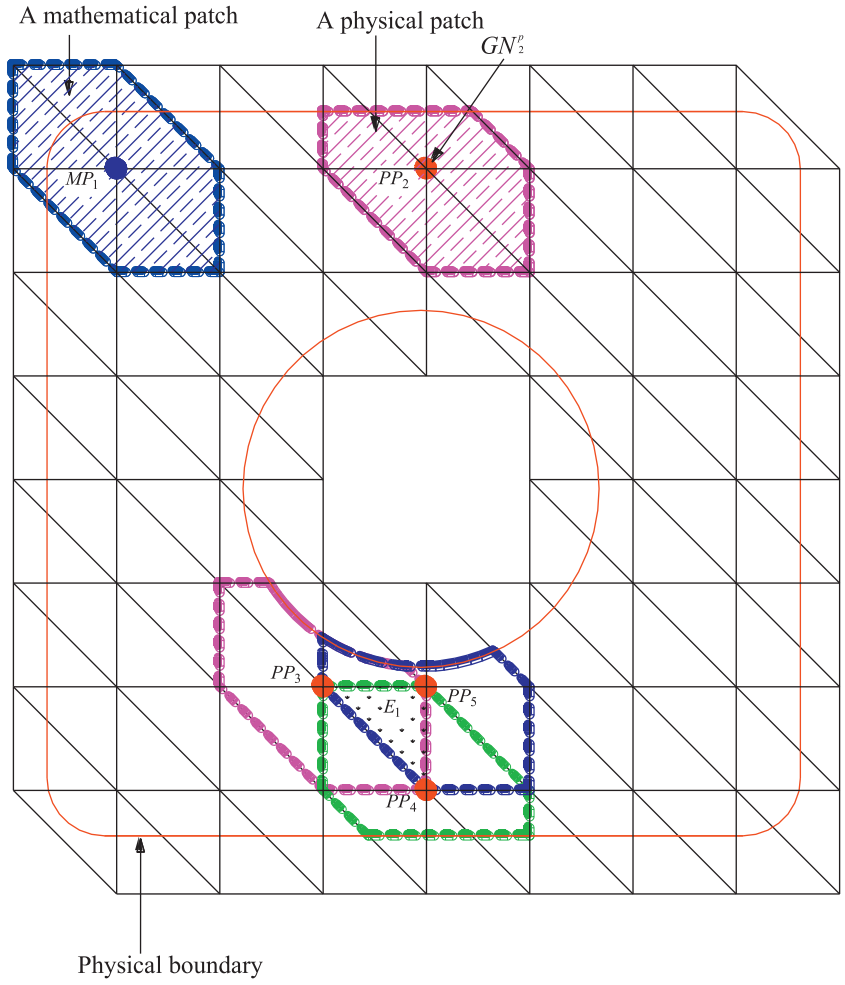

Fig. 1. Mathematical patches, physical patches and manifold elements in NMM.

$$w_1(\boldsymbol{x}) = L_1 + L_1^2 L_2 + L_1^2 L_3 - L_1 L_2^2 - L_1 L_3^2 \tag{4.1}$$

$$w_2(\boldsymbol{x}) = L_2 + L_2^2 L_3 + L_2^2 L_1 - L_2 L_3^2 - L_2 L_1^2 \tag{4.2}$$

$$w_3(\boldsymbol{x}) = L_3 + L_3^2 L_1 + L_3^2 L_2 - L_3 L_1^2 - L_3 L_2^2 \tag{4.3}$$

There are four important properties for the PU functions of iNMM:

(i) the PU condition: $\sum_{i=1}^{3} w_i(\boldsymbol{x}) = 1$,
(ii) non-negative property, $0 \le w_i(\boldsymbol{x}) \le 1$,
(iii) the Kronecker-delta property $w_i(\boldsymbol{x}_j) = \delta_{ij}$ $(i,j = 1,2,3)$.
(iv) the gradient of the PU functions is continuous at all the nodes.

3.2. Local approximation of the iNMM

There are mainly two ways to construct high order polynomial local approximations. Here, "high order" means the order of polynomial function is great than or equal to one. The first way is by using explicit polynomials (Eqs. (6)–(9)) to construct high order polynomial function, such as in standard GFEM or NMM. This, however, will not only significantly increase the global DOFs, but also lead to a LD problem. If the LD problem arises, traditional equation solver will fail and special equation solver is needed to solve the system equations. The second way is by using a meshfree method, which has been widely used in the "FE-Meshfree" elements [37]. In the second way, the number of global DOFs remains unchanged. Moreover, the LD problem will not arise. LSPIM [37], reduced CO-MLS (CO-LS) [43,44] and radial-polynomial basis functions [40], which possess the desired Kronecker-delta property, have been employed to construct the local approximation of 'FE-Meshfree' elements.

Since the LSPIM adopts pure polynomial basis functions to construct approximation, the singularity problem will appear if the nodes arrangement does not cooperate consistently with polynomial basis functions [51]. Therefore, the radial point interpolation method (RPIM) [40] is employed to construct the local approximation of the iNMM, because it combines the advantages of both radial basis functions and PIM, and is free from the singularity problem. The local approximation of iNMM, can then be expressed as

$$u_i(\boldsymbol{x}) = \sum_{j=1}^{n^{[i]}} r_j(x,y)a_j + \sum_{k=1}^{M} p_k(x,y)b_k = \mathbf{r}(x,y)\mathbf{a} + \mathbf{p}(x,y)\mathbf{b} \tag{5}$$

where M is the number of polynomial terms and $n^{[i]}$ is the total number of nodes in the domain of PP_i. $\mathbf{a}$ and $\mathbf{b}$ are two vectors yet to be determined. $\mathbf{p}(x, y)$ and $\mathbf{r}(x, y)$ denote polynomial functions and radial basis functions. Based on the value of M, $\mathbf{p}(x, y)$ can be expressed as

$$\text{If } M = 3, \boldsymbol{p}(\boldsymbol{x}) = \{1 \quad x \quad y\}; \tag{6}$$

$$\text{If } M = 4, \boldsymbol{p}(\boldsymbol{x}) = \{1 \quad x \quad y \quad xy\}; \tag{7}$$

$$\text{If } M = 6, \boldsymbol{p}(\boldsymbol{x}) = \{1 \quad x \quad y \quad xy \quad x^2 \quad y^2\}. \tag{8}$$

$$\text{If } M = 8, \boldsymbol{p}(\boldsymbol{x}) = \{1 \quad x \quad y \quad xy \quad x^2 \quad y^2 \quad x^2y \quad xy^2\} \tag{9}$$

In this study, the number of polynomial basis terms, M, is selected as follows: if $4 > n^{[i]} \geq 3$, $M=3$; if $5 \geq n^{[i]} \geq 4$, $M=4$; if $7 \geq n^{[i]} \geq 6$, $M=6$; if $n^{[i]} \geq 8$, $M=8$. The vector $\mathbf{r}(x, y)$ is expressed as [40]

$$\mathbf{r}(x,y) = [r_1(x,y)\ r_2(x,y)\ \cdots\ r_{n^{[i]}}(x,y)] \tag{10}$$

in which $r_j(x, y)$ is expressed as [52]

$$r_j(x,y) = (d_j^2 + c)^q \tag{11}$$

where $d_j(x,y) = \sqrt{(x-x_j)^2 + (y-y_j)^2}$, c and q are two parameters yet to be specified.

Enforcing Eq. (5) to pass through all the nodes in domain PP_i, the following equations are obtained:

$$\mathbf{u}_i = \mathbf{Ra} + \mathbf{Pb} \tag{12}$$

where $\mathbf{u}_i$ is a vector of corresponding nodal displacement of all the nodes in domain PP_i, the related matrix $\mathbf{R}$ and $\mathbf{P}$ are expressed as [40,52]

$$\mathbf{R} = \begin{bmatrix} r_1(x_1,y_1) & r_2(x_1,y_1) & \cdots & r_{n^{[i]}}(x_1,y_1) \\ r_1(x_2,y_2) & r_2(x_2,y_2) & \cdots & r_{n^{[i]}}(x_2,y_2) \\ \cdots & \cdots & \cdots & \cdots \\ r_1(x_{n^{[i]}},y_{n^{[i]}}) & r_2(x_{n^{[i]}},y_{n^{[i]}}) & \cdots & r_{n^{[i]}}(x_{n^{[i]}},y_{n^{[i]}}) \end{bmatrix} \tag{13}$$

$$\mathbf{P} = \begin{bmatrix} 1 & x_1 & y_1 & x_1^2 & x_1y_1 & y_1^2 \\ 1 & x_2 & y_2 & x_2^2 & x_2y_2 & y_2^2 \\ \vdots & \vdots & \vdots & \vdots & \vdots & \vdots \\ 1 & x_{n^{[i]}} & y_{n^{[i]}} & x_{n^{[i]}}^2 & x_{n^{[i]}}y_{n^{[i]}} & y_{n^{[i]}}^2 \end{bmatrix} (M=6, sosixcolumns) \tag{14}$$

Obviously, there are totally ($n^{[i]}$+M) parameters in Eq. (12). However, only $n^{[i]}$ equations are available. Nevertheless, according to the work finished by Liu and Gu [40] and Golberg et al. [53], vectors of $\mathbf{a}$ and $\mathbf{b}$ can be eliminated as proposed in their work and local approximation function in Eq. (5) is eventually expressed as [40]

$$u_i(x,y) = \mathbf{\Phi}_i\mathbf{u}_i, \quad i=1,2,3, \quad \mathbf{\Phi}_i = \mathbf{r}(x,y)\mathbf{S}_a + \mathbf{P}(x,y)\mathbf{S}_b \tag{15}$$

where

$$\mathbf{\Phi}_i = [\Phi_1^{[i]} \quad \Phi_2^{[i]} \quad \Phi_3^{[i]} \quad \cdots \quad \Phi_{n^{[i]}}^{[i]}] \tag{16}$$

$$\mathbf{u}_i = [u_1 \quad u_2 \quad u_3 \quad \cdots \quad u_{n^{[i]}}]^T \tag{17}$$

$$\begin{cases} \mathbf{S}_b = [\mathbf{P}^T\mathbf{R}^{-1}\mathbf{P}]^{-1}\mathbf{P}^T\mathbf{R}^{-1}, \\ \mathbf{S}_a = \mathbf{R}^{-1}[\mathbf{I} - \mathbf{PS}_b], \\ \mathbf{a} = \mathbf{S}_a\mathbf{u}_i, \\ \mathbf{b} = \mathbf{S}_b\mathbf{u}_i, \end{cases} \tag{18}$$

Notice that the evidence of the existence of R^{-1} for any scattered nodes has been given by Wendland [54].

3.3. Properties of shape function

The global approximation, $u^h(\boldsymbol{x})$, of iNMM presented in Eq. (1) can be rewritten in a simpler form:

$$u^h(\boldsymbol{x}) = \sum_{k=1}^{N} \varphi_k(\boldsymbol{x})a_k, \tag{19}$$

in which $\phi_k(\boldsymbol{x})$ is the shape function, a_k is the displacement parameter corresponding to node k and N ($N = \sum_{i=1}^{3} n^{[i]}$) is the total number of the nodes in the three PPs corresponding to the manifold element.

The shape function of iNMM has the following important properties:

(1) Kronecker-delta property

$$\varphi_i(\boldsymbol{x}_j) = \delta_{ij}. \tag{20}$$

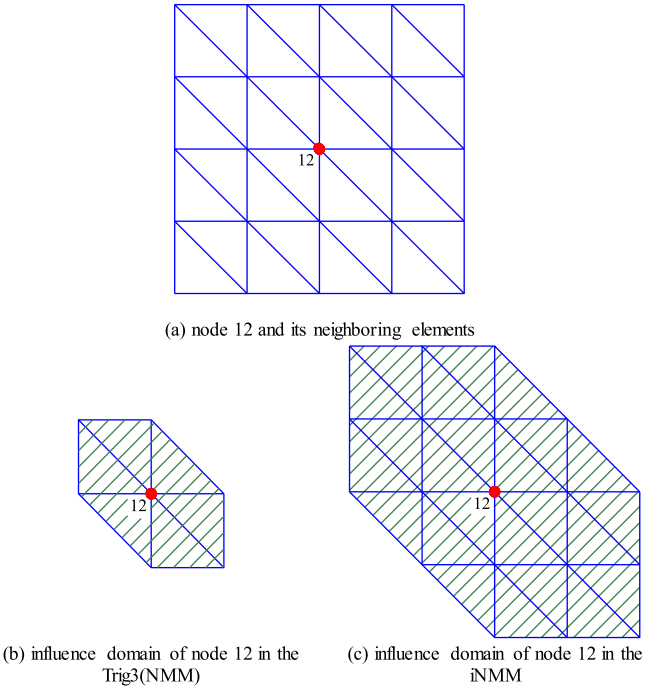

(a) node 12 and its neighboring elements

(b) influence domain of node 12 in the Trig3(NMM)

(c) influence domain of node 12 in the iNMM

Fig. 2. Comparison of the influence domain of node 12.

(2) Inter-element compatibility property.

(3) Higher order completeness properties i.e., reproducibility of all the monomial terms appearing in the assumed basis (Eqs. (6)–(9)).

(4) Derivatives of $u^h(\boldsymbol{x})$ are continuous at the nodes.

Shown in Fig. 2(a) is node 12 and its neighboring elements. It is noticed that the influence domain of node 12 in the iNMM is actually larger than that in the Trig3(NMM), as shown in Fig. 2(b) and (c). For the purpose of comparison, the plots of the PU functions and shape functions for the Trig3(NMM) and iNMM are all presented in Fig. 3. As can be seen from Fig. 3, the shape function of iNMM is much smoother than that of Trig3(NMM).

4. Discrete equations for iNMM

In the proposed iNMM, the displacement boundary conditions cannot be imposed directly as in FEM, because mathematical cover (MC) may not conform to the problem domain boundaries. Therefore, the displacement boundary conditions should be included into the potential energy by the Lagrange multiplier method or the penalty function method. For convenience, the developed iNMM adopts the penalty function method to impose the displacement boundary conditions, and the potential energy is expressed as

$$II(\boldsymbol{u}) = \int_\Omega \frac{1}{2}\boldsymbol{\epsilon}^T\boldsymbol{\sigma}d\Omega - \int_\Omega \boldsymbol{u}^T\boldsymbol{b}d\Omega - \int_{\Gamma_s} \boldsymbol{u}^T\bar{\boldsymbol{p}}dS + \int_{\Gamma_d} \frac{1}{2}\boldsymbol{k}(\boldsymbol{u}-\bar{\boldsymbol{u}})^T(\boldsymbol{u}-\bar{\boldsymbol{u}})dS \tag{21}$$

where Γ_s is the stress boundary, Γ_d is the displacement boundary, $\bar{\boldsymbol{u}}$ is the given displacement on Γ_d, $\bar{\boldsymbol{p}}$ is the given traction on Γ_s, $\boldsymbol{k}$ is the user-specified penalty, which can be set as 10^6E to obtain satisfactory accuracy. Here, E is the Young's modulus of the material closing to the displacement boundary.

The global displacement approximations expressed in Eq. (19) can be rewritten as

$$\boldsymbol{u} = \boldsymbol{N}\boldsymbol{h} \tag{22}$$

in which $\boldsymbol{N}$ is the shape function matrix, $\boldsymbol{h}$ is the vector including the degrees of freedom.

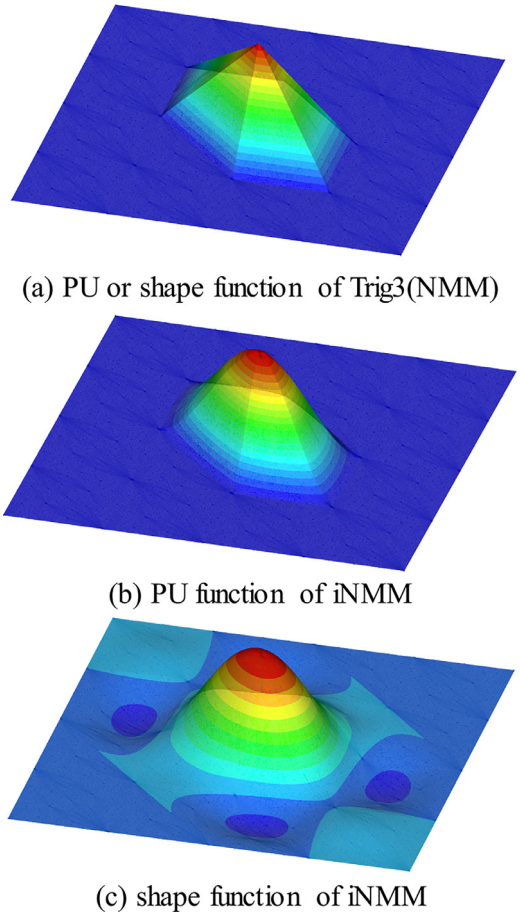

Fig. 3. Comparison of the PU and shape functions of Trig3(NMM) and iNMM.

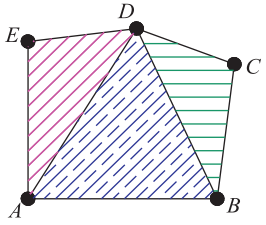

Fig. 4. Manifold elements divided into triangles to conduct Gaussian quadrature.

Substitution of the global displacement approximations (Eq. (22)) into Eq. (21), the system of equilibrium equations can then be expressed with the following matrix form:

$$\boldsymbol{K}\boldsymbol{p} = \boldsymbol{q} \tag{23}$$

in which $\boldsymbol{K}$ is the global stiffness matrix, $\boldsymbol{p}$ is the vector including all the degrees of freedom, $\boldsymbol{q}$ is the force vector. The global stiffness matrix $\boldsymbol{K}$ and force vector $\boldsymbol{q}$ will be formed by assembling all the element stiffness matrices $\boldsymbol{K}^e$ and element load vector $\boldsymbol{q}^e$, which are obtained by

$$\boldsymbol{K}^e = \int_{\Omega^e} \boldsymbol{B}^T \boldsymbol{D}\boldsymbol{B} d\Omega + \boldsymbol{k}\int_{\Gamma_d^e} \boldsymbol{N}^T\boldsymbol{N} dS \tag{24}$$

$$\boldsymbol{q}^e = \int_{\Omega^e} \boldsymbol{N}^T \boldsymbol{b} d\Omega + \int_{\Gamma_s^e} \boldsymbol{N}^T \bar{\boldsymbol{p}} dS + \boldsymbol{k}\int_{\Gamma_d^e} \boldsymbol{N}^T \bar{\boldsymbol{u}} dS \tag{25}$$

respectively.

Since the manifold element (Fig. 1) in iNMM can be in arbitrary shape, the manifold element should be firstly divided into a number of triangles (Fig. 4) and then Gauss quadrature rule is performed over each triangle.

5. Numerical examples

A set of numerical examples are carried out to assess the accuracy obtained through the iNMM. Since iNMM can always adopt regular mesh without considering the problem domain boundary to construct the global approximation, regular mathematical mesh for iNMM will always be used in the rest of this paper to conduct these tests. The physical units used in the present work are based on the international standard unit system. Here, n defines the total number of the nodes in the computational model. To assess accuracy and convergence, the relative L^2 errors in the displacement norm and in the energy norm are defined, respectively, as follows:

$$e_d = \sqrt{\frac{\int_\Omega (\boldsymbol{u}^{ex} - \boldsymbol{u}^{num})^2 d\Omega}{\int_\Omega (\boldsymbol{u}^{ex})^2 d\Omega}}, \tag{26}$$

$$e_e = \sqrt{\frac{\frac{1}{2}\int_\Omega (\varepsilon^{ex} - \varepsilon^{num})^T \boldsymbol{D}(\varepsilon^{ex} - \varepsilon^{num}) d\Omega}{\frac{1}{2}\int_\Omega (\varepsilon^{ex})^T \boldsymbol{D}(\varepsilon^{ex}) d\Omega}}, \tag{27}$$

where the superscript "ex" represents the exact or analytical solution and the superscript "num" denotes a numerical solution.

Apart from iNMM, the following examples will also be calculated by using the following numerical models, which are

(1) Quad4: Four-node isoparametric quadrilateral element.
(2) Quad8: Eight-node isoparametric quadrilateral element.
(3) NS-FEM: Node-based S-FEM based on triangular mesh [55].
(4) ES-FEM: Edge-based S-FEM based on triangular mesh [55].
(5) Trig3(NMM): Triangular mesh is employed to construct the MC, while the shape function of Trig3 is used to construct the PU, and constant for local approximation.
(6) Quad4(NMM): Quadrilateral mesh is employed to construct the MC, while the shape function of Quad4 is used to construct the PU, and constant for local approximation.

5.1. Linear dependence test

This example is employed to test whether the proposed iNMM suffers from the LD problem [33]. The material parameters employed for this example are Young's modulus $E = 1.0$ and Poisson's ratio $\nu = 0.25$. The plane stress condition is assumed. Fig. 5 shows all the meshes used for this example. Table 1 lists the number of computed zero eigenvalues obtained through the Trig3(NMM) and the proposed iNMM. According to the result from Table 1, before applying boundary condition, three zero eigenvalues (corresponding to the three rigid body modes) are found for all the meshes in both Trig3(NMM) and the iNMM. The number of zero eigenvalues is also found to be invariant with respect to the mesh geometry and mesh refinement. Furthermore, after applying the displacement boundary condition to eliminate the rigid body displacement, there are no more zero eigenvalues left, suggesting that the proposed iNMM is free of LD problem.

5.2. Cantilever beam subject to a tip-shear force

A 2D cantilever beam with length L, height D, and unit thickness is studied for the various behaviors of iNMM as a benchmark problem. As shown in Fig. 6, the cantilever beam is fixed at the left end and subjected to a parabolic traction P at the right end. The analytical solution is available in [56], and expressed as

$$u_x = \frac{Py}{6EI}\left[(6L - 3x)x + (2+\nu)(y^2 - \frac{D^2}{4})\right], \tag{28}$$

$$u_y = -\frac{P}{6EI}\left[3\nu y^2(L-x) + (4+5\nu)\frac{D^2 x}{4} + (3L-x)x^2\right], \tag{29}$$

where I is the moment of inertia for the beam with rectangular cross section and unit thickness.

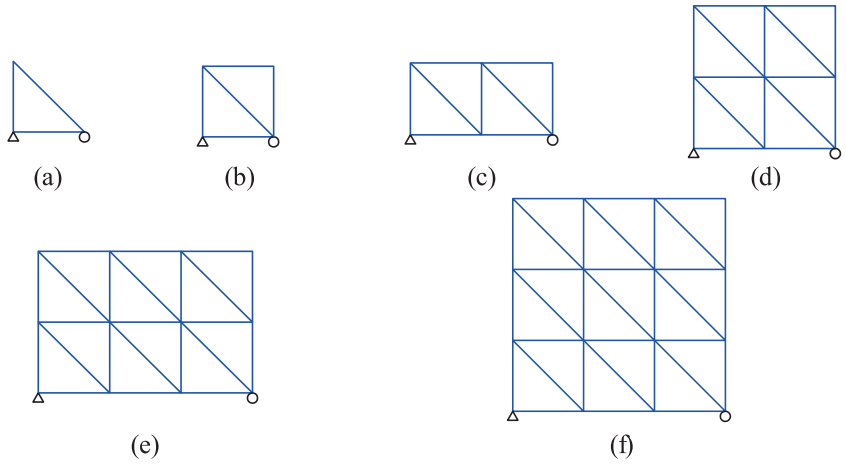

Fig. 5. Meshes employed in iNMM to test the LD issue (△-constrains in both the x- and y-directions, ○-constrains in the y-direction).

Table 1
Nullity of stiffness matrices of Trig3(NMM) and iNMM, see Fig. 5 for the meshes.

Mesh	Total DOfs	Trig3(NMM)		iNMM	
		Nullity DOfs (without essential boundary treatment)	Nullity DOfs (apply essential boundary treatment)	Nullity DOfs (without essential boundary treatment)	Nullity DOfs (apply essential boundary treatment)
(a)	6	3	0	3	0
(b)	8	3	0	3	0
(c)	12	3	0	3	0
(d)	18	3	0	3	0
(e)	24	3	0	3	0
(f)	32	3	0	3	0

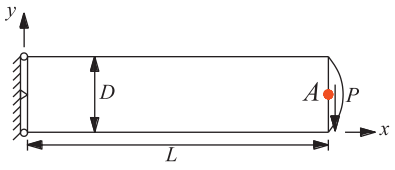

Fig. 6. A cantilever beam subjected to a tip-shear force on the right end.

The stress corresponding to the displacements are

$$\sigma_{xx}(x,y)=\frac{P(L-x)y}{I},\quad \sigma_{yy}(x,y)=0,\quad \tau_{xy}(x,y)=-\frac{P}{2I}\left(\frac{D^2}{4}-y^2\right). \tag{30}$$

The geometric and mechanical parameters for this example are $L=48$, $D=12$, $E=3.0\times10^7$ and $\nu=0.3$. The load $P=1000$, and the plane stress condition is assumed. In the computation, the points on the boundary of $x=0$ are constrained using the exact displacements given from the analytical solutions, and the traction is specified on the boundary at $x=L$ using the analytical solutions.

5.2.1. Effect of parameters c *and* q

The values of c and q will affect the performance of RPIM [40,52], and hence obtaining the optimal values for c and q in terms of iNMM is very important. In Dinis's work [57,58], it was found that higher accuracy is obtained if $c\to0.0$ and $q\to1.0$. In Liu's work [40], good results are obtained when $c=1.0$ and $q=1.03$ for the free vibration problem, while in Xu and Rajendran's work [59], good results are obtained when $c=0.0001$ and $q=2.01$ for the static problems.

In this study, various values of parameters c and q are used to test their influence on the accuracy of the proposed method. The discrete model presented in Fig. 7(a) is adopted. Results obtained through iNMM in both displacement norm and energy norm are plotted in Fig. 8. In addition, deflection of point A versus q is also plotted, as shown in Fig. 9. As can be seen from Figs. 8 and 9, good results are obtained when $c=0.0001$ and $q=2.01$. For all the computations hereon, the optimal parameter combination, with $c=0.0001$, $q=2.01$, will be used.

5.2.2. Convergence study

In order to investigate the convergence of solution by iNMM, four discrete models with regular grids are constructed as shown in Fig. 7. The convergence curves are plotted in Fig. 10. Accuracy ob-

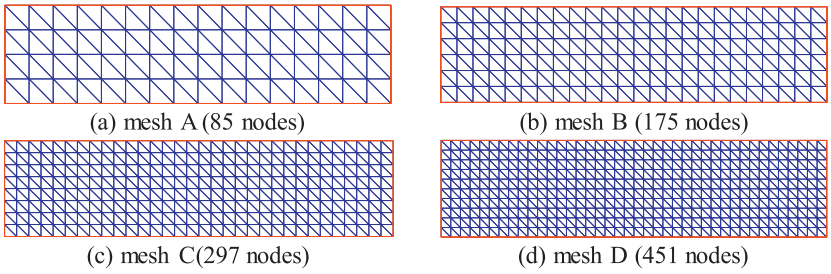

Fig. 7. Mesh for cantilever beam subjected to a tip-shear force.

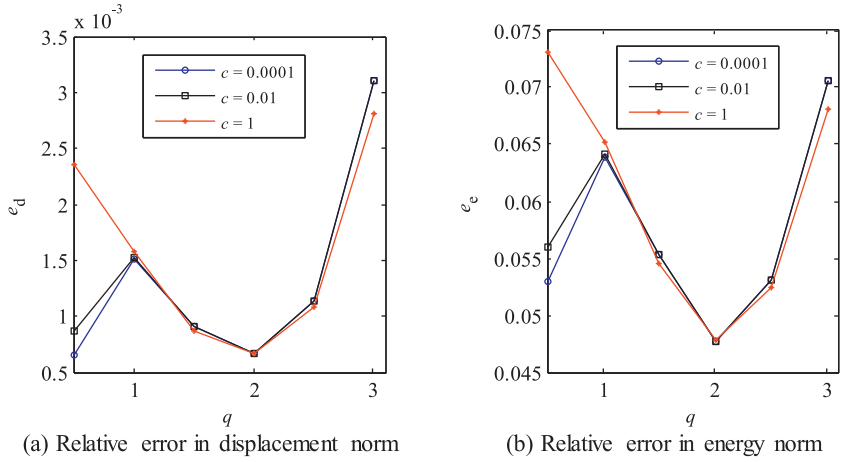

Fig. 8. Relative error in displacement and energy norms versus q in the cantilever beam problem subjected to a tip-shear force.

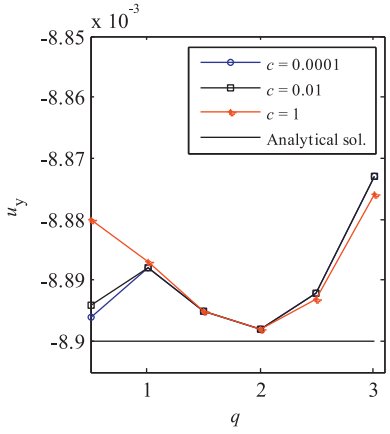

Fig. 9. Deflection of point A versus q in the cantilever beam problem subjected to a tip-shear force.

tained through iNMM in both displacement norm and energy norm are compared to that obtained through Trig3(NMM) and Quad4(NMM). As can be seen from Fig. 10, the numerical results obtained through the proposed iNMM are significantly better than those obtained through Trig3(NMM) and Quad4(NMM) in both displacement norm and energy norm.

The contour plot of σ_x on the regular mesh for Trig3(NMM), Quad4(NMM) and iNMM is plotted in Fig. 11. It can be found that the

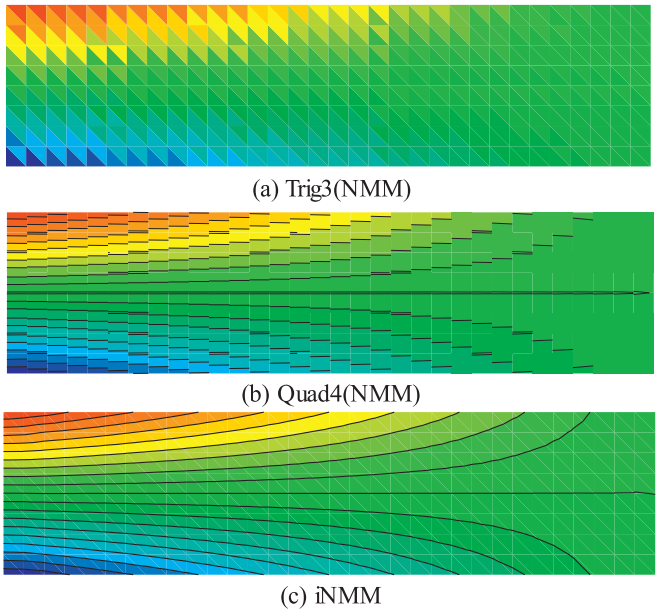

Fig. 11. Contour plot of σ_x for the cantilever beam subjected to a tip-shear force (see Fig. 7(c) for the mesh).

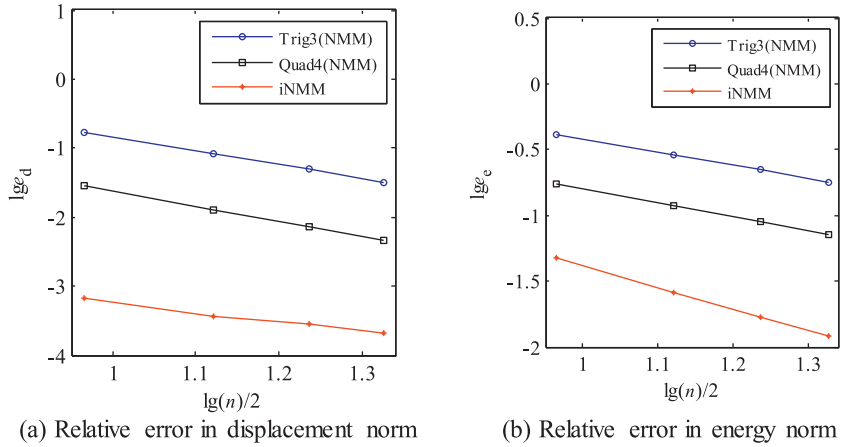

Fig. 10. Comparison of accuracy for cantilever beam problem subjected to a tip-shear force.

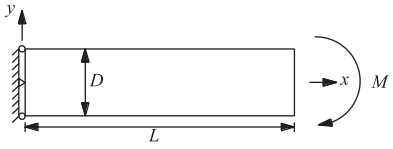

Fig. 12. A 2D cantilever beam subjected to a tip-moment.

global stress field obtained through iNMM is much smoother than that obtained through Trig3(NMM) and Quad4(NMM).

5.3. Cantilever beam subject to a tip-moment

A cantilever beam subjected a tip-moment is considered in this section, as shown in Fig. 12. The geometric and mechanical parameters for this example are $D = 12$, $L = 48$, Young's modulus $E = 3.0\times 10^7$ and Poisson's ratio $\nu = 0.3$. The bending moment $M = 2.4 \times 10^4$, and the plane stress condition is assumed. The analytical solution for this example can be found in [56].

For the purpose of studying the convergence of solution by iNMM, this example also adopts the four discrete models (Fig. 7) presented in Section 5.2. The convergence curves in terms of displacement norm and energy norm are plotted in Fig. 13. As can be seen from Fig. 13, the numerical results obtained through the proposed iNMM are significantly better than those obtained through Trig3(NMM) and Quad4(NMM) in both displacement norm and energy norm.

In addition, the contour plot of σ_x obtained through Trig3(NMM) and iNMM is plotted in Fig. 14. It can be found that the global stress field obtained through the proposed iNMM is smoother than that obtained through Trig3(NMM).

5.4. Cook's skew beam

As shown in Fig. 15(a), Cook's skew beam [59] is taken as an example in this section. Fig. 15(b) gives an example mesh for Trig3(NMM) and iNMM with 4×4 layers (Part of the mathematical mesh which will not be used has been discarded) and 22 nodes for this problem, while Fig. 15(c) gives an example mesh for node-based S-FEM (NS-FEM) and edge-based S-FEM (ES-FEM) [55] with 4×4 layers and 25 nodes, Fig. 15(d) gives an example mesh for Quad4 (25 nodes) and Quad8 (65 nodes) with 4×4 layers, and Fig. 15(e) gives an example mesh for Quad4(NMM) with 4×4 layers (part of mathematical mesh which will not be used has been discarded) and 22 nodes.

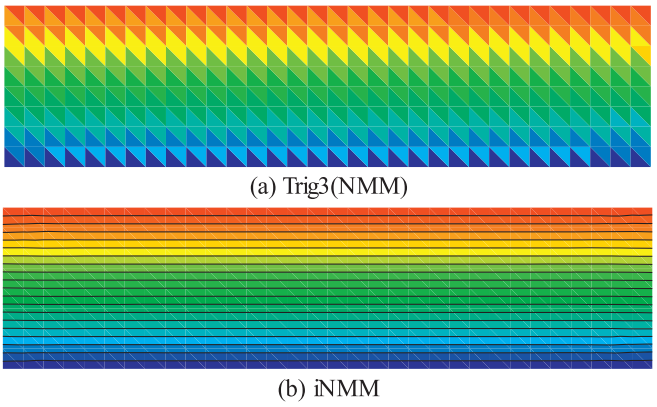

Fig. 14. Contour plot of σ_x for cantilever beam subjected to a tip-moment (see Fig. 7(c) for the mesh).

Table 2
Vertical displacement v_A for point A for Cook's skew beam.

Element type		Mesh			
		4×4	8×8	16×16	32×32
Quad4	n	25	81	289	1089
	V_A	18.29	22.08	23.43	23.82
ES-FEM	n	25	81	289	1089
	V_A	19.72	22.74	23.65	23.88
NS-FEM	n	25	81	289	1089
	V_A	26.41	24.85	24.24	24.05
Quad8	n	65	225	833	3201
	V_A	23.71	23.88	23.93	23.96
Trig3(NMM)	n	22	60	183	622
	V_A	16.93	21.20	23.07	23.70
Quad4(NMM)	n	22	60	183	622
	V_A	19.72	22.56	23.54	23.85
iNMM	n	22	60	183	622
	V_A	22.42	23.80	23.93	23.96
Reference	23.96				

The numerical results of 4 types of mesh obtained through the proposed iNMM and other numerical models including Trig3(NMM), Quad4(NMM), Quad4, Quad8, NS-FEM and ES-FEM, are listed together in Table 2. For the purpose of observation, the calculated displacements versus n (the number of nodes) from Table 2 are also plotted in Fig. 16.

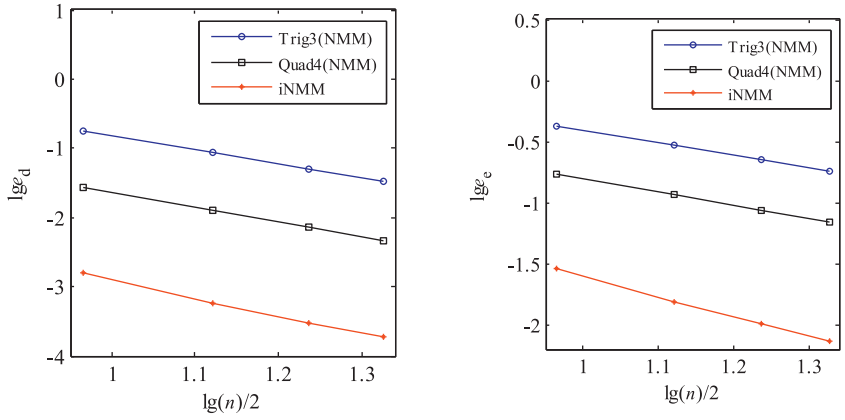

(a)Relative error in displacement norm (b)Relative error in energy norm

Fig. 13. Comparison of accuracy for cantilever beam problem subjected to a tip-moment.

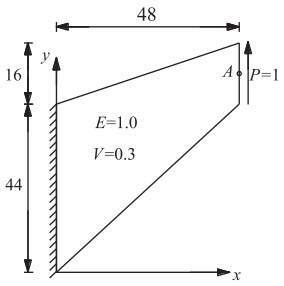

(a) The geometry and the boundary conditions

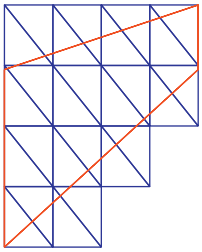

(b) example mesh for Trig3(NMM) and the iNMM with 4×4 layers and 22 nodes

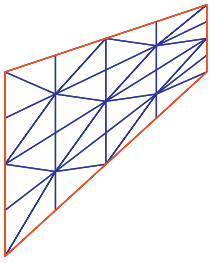

(c) example mesh for ES-FEM and NS-FEM with 4×4 layers and 25 nodes

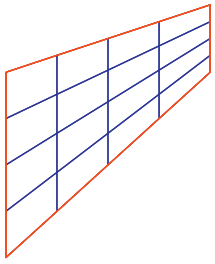

(d) example mesh for Quad4 element with 4×4 layers and 25 nodes

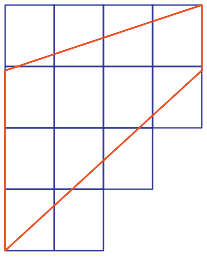

(e) example mesh for Quad4(NMM) with 4×4 layers and 22 nodes

Fig. 15. Cook's skew beam.

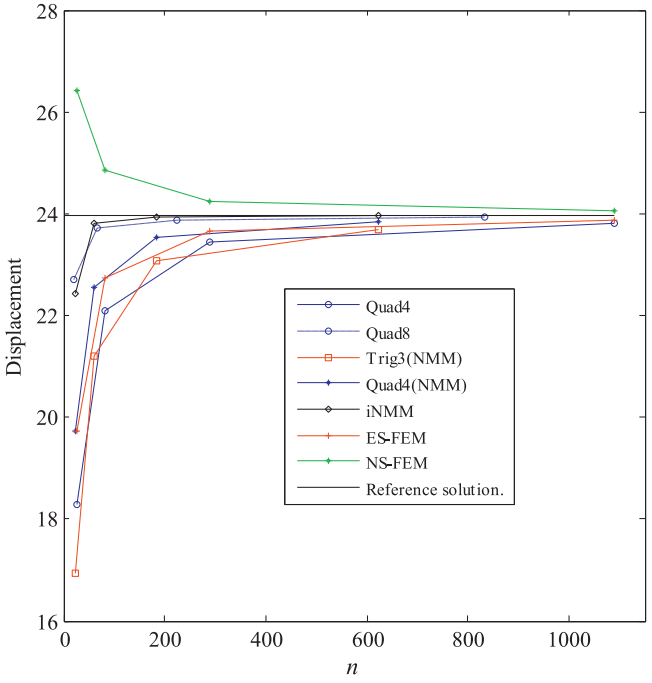

Fig. 16. Displacement of Cook's skew beam.

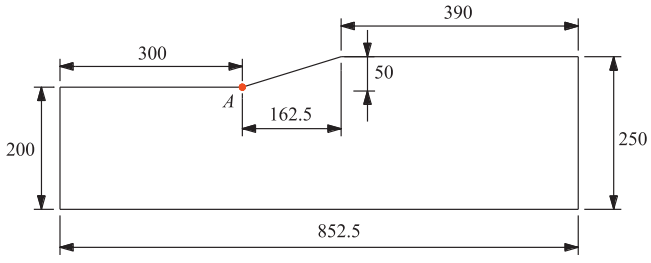

Fig. 17. Dimensions of slope model [41].

As can be seen in Fig. 16, the results obtained through the proposed iNMM are much better than those obtained through Trig3(NMM), Quad4(NMM), Quad4, NS-FEM and ES-FEM. In addition, the iNMM gives results comparable to those obtained through Quad8. It is noticed that Quad8 is very sensitive to mesh quality [41]. Often in practice, it is very difficult to generate high quality mesh for problems with complex geometry. But, the proposed iNMM is free from this problem, because it can always adopt regular mathematical mesh without considering the problem domain boundary to discretize the problem domain.

5.5. Slope

In this section, a homogeneous slope [41] subjected to self-weight is considered, as shown in Fig. 17. The bottom of the slope is fixed,

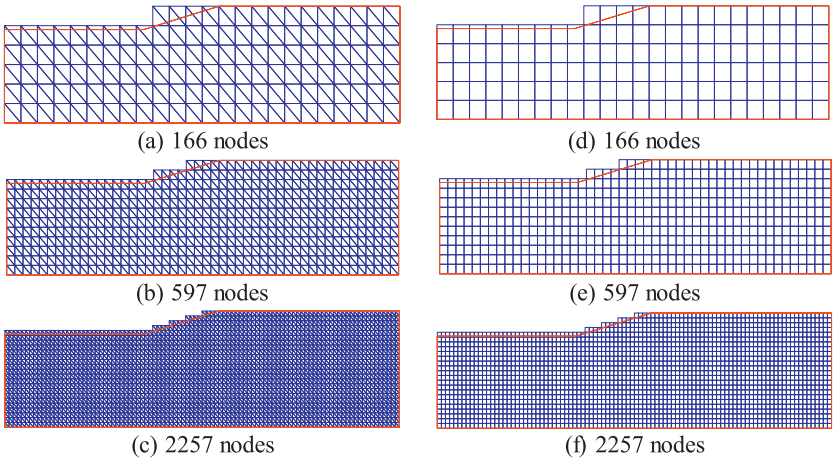

Fig. 18. Discretized models of a slope.

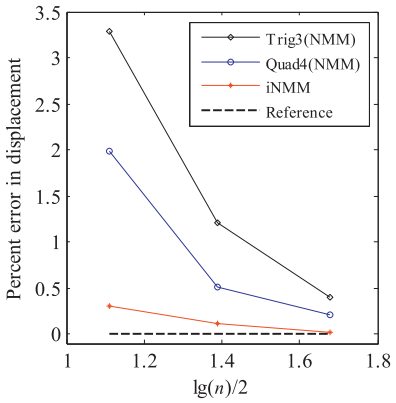

Fig. 19. Vertical displacement errors of point *A*.

while the left and right sides are subjected to normal constraint. In the computation, the material parameters are assumed as Young's modulus $E = 8 \times 10^7$, Poisson's ratio $\nu = 0.43$ and unit weight $\gamma = 1.962 \times 10^4$. The discretized models for this example are shown in Fig. 18. The reference solution for the vertical displacement of point *A* is −1.6068 [41].

The vertical displacement errors of point *A* versus *n* obtained by Trig3(NMM), Quad4(NMM) and the proposed iNMM are plotted in Fig. 19. As can be seen from Fig. 19, the proposed iNMM obtained much better results than Trig3(NMM) and Quad4(NMM).

5.6. A rectangular plate with two holes

A rectangular plate with two holes is considered in this example, as shown in Fig. 20. The bottom of the plate is constrained in normal direction. Only the midpoint of the bottom is fixed. The upside of the plate is subjected to a uniformly distributed load. In the computation, the material parameters are assumed as Young's modulus $E = 3 \times 10^7$, Poisson's ratio $\nu = 0.3$ and $P = 1$. The plane stress condition is assumed. The discretized models for Trig3(NMM) and iNMM are shown in Fig. 21(a)–(c), while the discretized models for Quad4(NMM) are shown in Fig. 21(d)–(f). Due to the lack of theoretical solution, the problem domain is discretized with very fine mesh with 18,147 nodes, as shown in Fig. 22. A reference solution is calculated by Quad4(NMM) using this discretized model. The reference solution for the vertical displacement of point *A* is 1.064×10^{-6}.

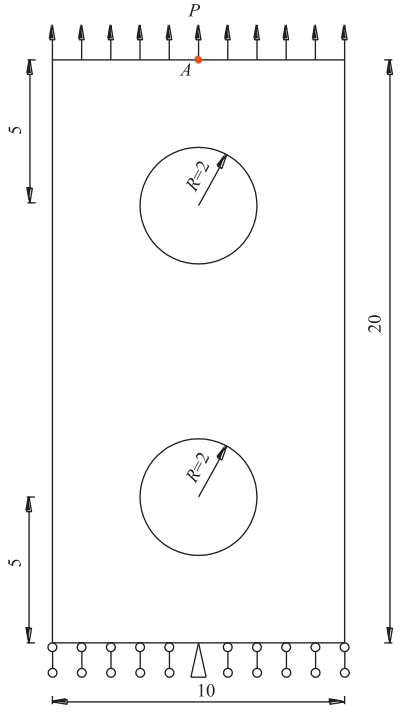

Fig. 20. Dimensions of a rectangular plate with two holes.

The vertical displacement errors of point *A* versus *n* obtained by Trig3(NMM), Quad4(NMM) and the proposed iNMM are plotted in Fig. 23. As can be seen from Fig. 23, the proposed iNMM obtained much better results than Trig3(NMM) and Quad4(NMM).

6. Discussions and conclusions

In this study, an improved version of numerical manifold method (iNMM) has been proposed. The proposed iNMM performs excellently for linear elastic problems of two dimensional solid. Some important observations from this work are as follows:

(1) In the iNMM, high-order global approximation can be constructed without extra nodes or DOFs. The shape function of

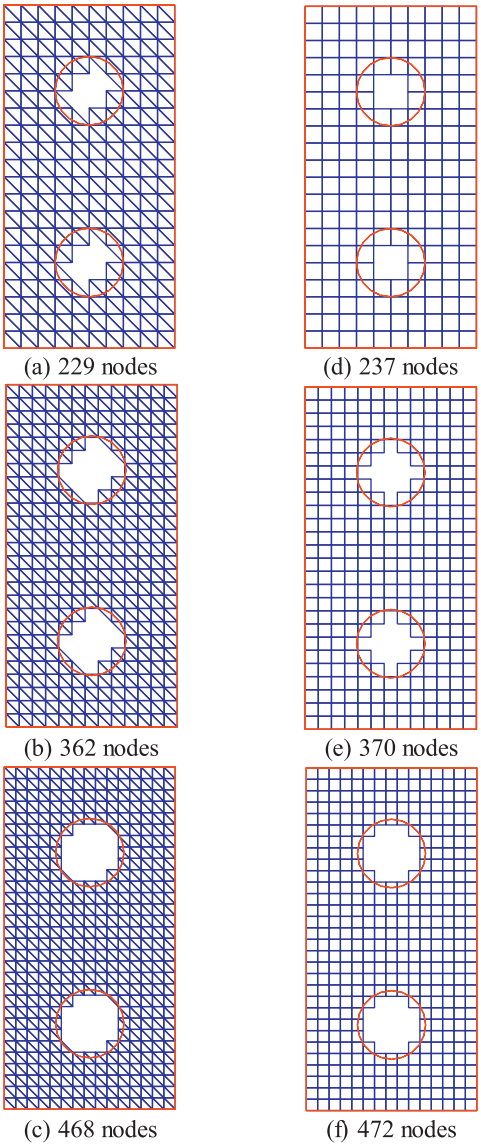

Fig. 21. Discretized models of the plate with two holes.

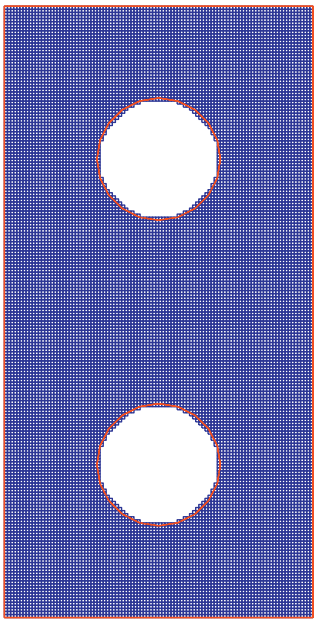

Fig. 22. Discretized model of the plate with two holes to obtain reference solution (18,147 nodes).

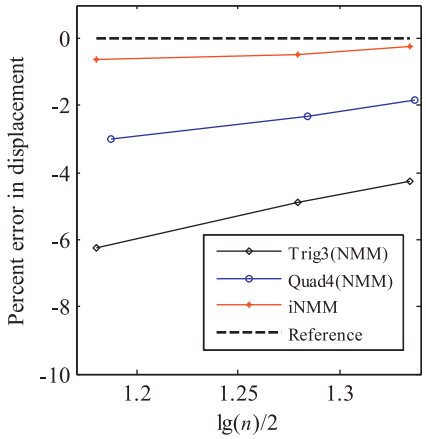

Fig. 23. Vertical displacement errors of point *A* for the rectangular plate with two holes.

iNMM processes the much desired Kronecker-delta property. Moreover, the proposed iNMM is free from the LD problem.

(2) The stress field obtained through iNMM is continuous at the nodes. With this advantage, the nodal stress can be conveniently obtained without any smoothing operation.

(3) Inheriting all the advantage from numerical manifold method (NMM), the iNMM can always adopt regular mesh without considering the problem domain boundary to discretize the problem domain.

(4) Accuracy obtained through the proposed iNMM is significantly better than that obtained through Trig3(NMM), Quad4(NMM), Quad4, NS-FEM and ES-FEM.

In view of the advantages of the iNMM, it is worth to further study and apply it to other fields. It is noticed the present work is still very preliminary. In the following work, we will apply the present iNMM to simulate multiple crack propagation problems.

Acknowledgment

This study is supported by the National Natural Science Foundation of China, under the Grant nos. 51609240, 11572009, 51538001, 51579235 and 41472288; and the National Basic Research Program of China (973 Program), under the Grant no. 2014CB047100.

References

[1] Xu DD, Yang YT, Zheng H, Wu AQ. A high order local approximation free from linear dependency with quadrilateral mesh as mathematical cover and applications to linear elastic fractures. Comput Struct 2017;178:1–16.

[2] Babuška I, Melenk JM. The partition of unity method. Int J Numer Methods Eng 1997;40:727–58.

[3] Melenk JM, Babuška I. The partition of unity finite element method: basic theory and applications. Comput Methods Appl Mech Eng 1996;139(1-4):289–314.

[4] Zheng H, Yang YT. On generation of lumped mass matrices in partition of unity based methods. Int J Numer Methods Eng. doi:10.1002/nme.5544.

[5] Rabczuk T, Bordas S, Zi G. On three-dimensional modelling of crack growth using partition of unity methods. Comput Struct 2010;88(23):1391–411.

[6] Strouboulis T, Babuška I, Copps K. The design and analysis of the generalized finite element method. Comput Methods Appl Mech Eng 2000;181(1):43–69.

[7] Belytschko T, Black T. Elastic crack growth in finite elements with minimal remeshing. Int J Numer Methods Eng 1999;45(5):601–20.

[8] Amiri F, Anitescu C, Arroyo M, Bordas S, Rabczuk T. XLME interpolants, a seamless bridge between XFEM and enriched meshless methods. Comput Mech 2014;53(1):45–57.
[9] Shi GH. Manifold method of material analysis. In: Proceedings of the transcations of the ninth army conference on applied mathematics and computing; 1991. p. 57–76.
[10] Yang YT, Sun GH, Cai KJ, Zheng H. A high order numerical manifold method and its application to linear elastic continuous and fracture problems. Sci China Technol Sci doi:10.1007/s11431-016-9070-8.
[11] Chau-Dinh T, Zi G, Lee PS, Rabczuk T, Song JH. Phantom-node method for shell models with arbitrary cracks. Comput Struct 2012;92:242–56.
[12] Rabczuk T, Zi G, Gerstenberger A, Wall WA. A new crack tip element for the phantom-node method with arbitrary cohesive cracks. Int J Numer Methods Eng 2008;75(5):577–99.
[13] Rabczuk T, Zi G, Bordas S, Nguyen-Xuan H. A simple and robust three-dimensional cracking-particle method without enrichment. Comput Methods Appl Mech Eng 2010;199(37):2437–55.
[14] Rabczuk T, Belytschko T. Cracking particles: a simplified meshfree method for arbitrary evolving cracks. Int J Numer Methods Eng 2004;61(13):2316–43.
[15] Rabczuk T, Belytschko T. A three-dimensional large deformation meshfree method for arbitrary evolving cracks. Comput Methods Appl Mech Eng 2007;196(29):2777–99.
[16] Ghorashi SS, Valizadeh N, Mohammadi S, Rabczuk T. T-spline based XIGA for fracture analysis of orthotropic media. Comput Struct 2015;147:138–46.
[17] Yang YT, Zheng H, Sivaselvan MV. A rigorous and unified mass lumping scheme for higher-order elements. Comput Methods Appl Mech Eng 2017;319:491–514.
[18] Zheng H, Liu F, Du XL. Complementarity problem arising from static growth of multiple cracks and MLS-based numerical manifold method. Comput Methods Appl Mech Eng 2015;295:150–71.
[19] Ma GW, An XM, Zhang HH, Li LX. Modelling complex crack problems using the numerical manifold method. Int J Fract 2009;156:21–35.
[20] Yang YT, Tang XH, Zheng H, He L. Three-dimensional fracture propagation with numerical manifold method. Eng Anal Bound Elem 2016;72:65–77.
[21] Yang YT, Zheng H. A three-node triangular element fitted to numerical manifold method with continuous nodal stress for crack analysis. Eng Fract Mech 2016;162:51–75.
[22] Yang YT, Xu DD, Sun GH, Zheng H. Modeling complex crack problems using the three-node triangular element fitted to numerical manifold method with continuous nodal stress. Sci China Technol Sci doi:10.1007/s11431-016-0733-4.
[23] Yang YT, Sun GH, Zheng H, Fu XD. A four-node quadrilateral element fitted to numerical manifold method with continuous nodal stress for crack analysis. Comput Struct 2016;177:69–82.
[24] Wu ZJ, Wong LNY, Fan LF. Dynamic study on fracture problems in viscoelastic sedimentary rocks using the numerical manifold method. Rock Mech Rock Eng 2013;46(6):1415–27.
[25] Yang YT, Zheng H. Direct approach to treatment of contact in numerical manifold method. ASCE Int J Geomech 2016:E4016012.
[26] Jiang QH, Deng SS, Zhou CB, Lu WB. Modeling unconfined seepage flow using three--dimensional numerical manifold method. J Hydrodyn 2010;22:554–61.
[27] Zheng H, Liu F, Li CG. Primal mixed solution to unconfined seepage flow in porous media with numerical manifold method. Appl Math Model 2015;39:794–808.
[28] Wu ZJ, Fan LF. The numerical manifold method for elastic wave propagation in rock with time-dependent absorbing boundary conditions. Eng Anal Bound Elem 2014;46:41–50.
[29] He L, An X, Liu X, et al. Augmented numerical manifold method with implementation of flat-top partition of unity. Engg Anal Bound Elem 2015;61:153–71.
[30] Schweitzer M A. Generalizations of the finite element method. Central Eur J Math 2012;10(1):3–24.
[31] An XM, Li LX, Ma GW, et al. Prediction of rank deficiency in partition of unity-based methods with plane triangular or quadrilateral meshes. Comput Methods Appl Mech Eng 2011;200(5):665–74.
[32] Griebel M, Schweitzer MA. A particle-partition of unity methods. Part VII: Adaptivity, meshfree methods for partial differential equations III. Lecture notes in computational science and engineering, vol. 57. Springer; 2007.
[33] Tian R, Yagawa G, Terasaka H. Linear dependence problems of partition of unity-based generalized FEMs. Comput Methods Appl Mech Eng 2006;195(37-40):4768–82.
[34] Cai Y, Zhuang X, Augarde C. A new partition of unity finite element free from the linear dependence problem and possessing the delta property. Comput Methods Appl Mech Eng 2010;199(17):1036–43.
[35] Riker C, Holzer S M. The mixed-cell-complex partition-of-unity method. Comput Methods Appl Mech Eng 2009;198(13):1235–48.
[36] Rajendran S, Zhang BR. A "FE-meshfree" QUAD4 element based on partition of unity. Comput Methods Appl Mech Eng 2007;197(1-4):128–47.
[37] Xu JP, Rajendran S. A 'FE-Meshfree' TRIA3 element based on partition of unity for linear and geometry nonlinear analyses. Comput Mech 2013;51(6):843–64.
[38] Yang YT, Xu DD, Zheng H. A partition-of-unity based 'FE-Meshfree' triangular element with radial-polynomial basis functions for static and free vibration analysis. Eng Anal Bound Elem 2016;65:18–38.
[39] Yang YT, Tang XH, Zheng H. Construct 'FE-Meshfree' Quad4 using mean value coordinates. Eng Anal Bound Elem 2015;59:78–88.
[40] Liu G, Gu YT. A local radial point interpolation method (LRPIM) for free vibration analyses of 2-d solids. J Sound Vib 2001;246(1):29–46.
[41] Yang YT, Bi R, Zheng H. A hybrid 'FE-Meshless' QUAD4 with continuous nodal stress using radial-polynomial basis functions. Eng Anal Bound Elem 2015;53:73–85.
[42] Yang YT, Sun GH, Zheng H. Application of the 'FE-Meshfree' QUAD4 with continuous nodal stress using radial-polynomial basis functions for vibration and geometric nonlinear analyses. Eng Anal Bound Elem. doi:10.1016/j.enganabound.2017.02.007.
[43] Tang XH, Zheng C, Wu SC, Zhang JH. A novel four-node quadrilateral element with continuous nodal stress. Appl Math Mech (English Edition) 2009;30(12):1519–32.
[44] Yang YT, Tang XH, Zheng H. A three-node triangular element with continuous nodal stress. Comput Struct 2014;141:46–58.
[45] Yang YT, Chen L, Tang XH, Zheng H. A partition-of-unity based 'FE-Meshfree' hexahedral element with continuous nodal stress. Comput Struct 2017;178:17–28.
[46] Yang YT, Xu DD, Zheng H. Application of the three-node triangular element with continuous nodal stress for free vibration analysis. Comput Struct 2016;169:69–80.
[47] Yang YT, Chen L, Xu DD, Zheng H. Free and forced vibration analyses using the four-node quadrilateral element with continuous nodal stress. Eng Anal Bound Elem 2016;70:1–11.
[48] Yang YT, Zheng H, Xu DD. A partition-of-unity based three-node triangular element with continuous nodal stress using radial-polynomial basis functions. Sci China Technol Sci, doi:10.1007/s11431-016-9020-3.
[49] Zheng H, Xu DD. New strategies for some issues of numerical manifold method in simulation of crack propagation. Int J Numer Methods Eng 2014;97(13):986–1010.
[50] Zienkiewicz OC, Taylor RL. The finite element method. 5th ed. Oxford: Butterworth-Heinemann; 2000.
[51] Wang JG, Liu GR. A point interpolation meshless method based on radial basis functions. Int J Numer Methods Eng 2002;54(11):1623–48.
[52] Liu GR. Mesh free methods: moving beyond the finite element method. Boca Raton, USA: CRC Press; 2003.
[53] Golberg MA, Chen CS, Bowman H. Some recent results and proposals for the use of radial basis functions in the BEM. Eng Anal Bound Elem 1999;23:285–96.
[54] Wendland H. Error estimates for interpolation by compactly supported radial basis functions of minimal degree. J Approx Theory 1998;93(2):258–72.
[55] Liu GR, Nguyen-Thoi T. Smoothed finite element methods. New York: CRC Press; 2010.
[56] Timoshenko SP, Goodier JN. Theory of elasticity. 3rd ed. New York, U.K.: Mcgraw-Hill College; 1970.
[57] Dinis L, Natal Jorge R M, Belinha J. Composite laminated plates: a 3D natural neighbor radial point interpolation method approach. J Sandw Struct Mater 2010;12(2):119–38.
[58] Dinis L, Jorge R M N, Belinha J. Analysis of 3D solids using the natural neighbour radial point interpolation method. Comput Methods Appl Mech Eng 2007;196(13):2009–28.
[59] Xu JP, Rajendran S. A partition-of-unity based 'FE-Meshfree' QUAD4 element with radial-polynomial basis functions for static analyses. Comput Methods Appl Mech Eng 2011;200(47–48):3309–23.